Experimental Mechanics (2007) 47: 25–36
DOI 10.1007/s11340-006-9344-6

Modulus, Fracture Strength, and Brittle vs. Plastic Response of the Outer Shell of Arc-grown Multi-walled Carbon Nanotubes

W. Ding · L. Calabri · K.M. Kohlhaas · X. Chen · D.A. Dikin · R.S. Ruoff

Received: 27 March 2006 / Accepted: 25 May 2006 / Published online: 1 August 2006

Abstract The fracture strengths and elastic moduli of arc-grown multi-walled carbon nanotubes (MWCNTs) were measured by tensile loading inside of a scanning electron microscope (SEM). Eighteen tensile tests were performed on 14 MWCNTs with three of them being tested multiple times (3×, 2×, and 2×, respectively). All the MWCNTs fractured in the "sword-in-sheath" mode. The diameters of the MWCNTs were measured in a transmission electron microscope (TEM), and the outer diameter with an assumed 0.34 nm shell thickness was used to convert measured load-displacement data to stress and strain values. An unusual yielding before fracture was observed in two tensile loading experiments. The 18 outer shell fracture strength values ranged from 10 to 66 GPa, and the 18 Young's modulus values, obtained from a linear fit of the stress–strain data, ranged from 620 to 1,200 GPa, with a mean of 940 GPa. The possible influence of stress concentration at the clamps is discussed.

Keywords Nanotube · Fracture · Yield · Modulus · Strength

W. Ding · K.M. Kohlhaas · X. Chen · D.A. Dikin
R.S. Ruoff (✉)
Department of Mechanical Engineering,
Northwestern University,
Evanston, IL 60208, USA
e-mail: r-ruoff@northwestern.edu

L. Calabri
CNR-INFM-National Research on nanoStructures
and bioSystems at Surfaces (S3),
via Campi 213/a,
4100 Modena, Italy

Introduction

The experimental discovery of multi-walled carbon nanotubes (MWCNTs) in 1991 [1] and single-walled carbon nanotubes (SWCNTs) in 1993, [2, 3] has spawned considerable interest in carbon nanotubes. Theoretical studies have predicted that defect-free CNTs should have a Young's modulus of ~1 TPa, [4–6] similar to the in-plane modulus of graphite (if a shell thickness of 0.34 nm is used). Among numerous examples, MWCNTs have been studied in nanoscale devices, [7–9] and as filler in composites [10–12]. The mechanical properties of CNTs are clearly of both intrinsic and practical importance.

Several techniques have been developed for exploring the mechanical properties of individual CNTs. For example, the elastic moduli of cantilevered MWCNTs were obtained from mechanical resonance observed inside a TEM [13–16]. The elastic moduli of MWCNTs deposited across pores on an alumina nanopore membrane were obtained from bending tests carried out with an AFM, [17] and the same approach was used to obtain the elastic and shear moduli of SWCNT ropes [18]. The fracture strengths and elastic moduli of MWCNTs [19] and SWCNT ropes [20] have been obtained by tensile testing inside a SEM.

We present a detailed study of the mechanical properties of arc-grown MWCNTs by tensile loading inside an SEM. Individual MWCNTs were tensile loaded until fracture by using a piezo-actuated nanomanipulator [21]. The fracture strengths, failure strains and elastic moduli of the MWCNTs were obtained from the measured geometry, the load at failure, and the load-displacement (which with the measured geometry is converted to stress–strain) data. No

slippage was observed at the clamps during or after the tensile loading process. Three MWCNTs were tensile loaded multiple times and an increase of the measured fracture strength was observed upon loading of the fragments resulting from prior fracture.

Experiment

Material

The MWCNT material was acquired from MER Corporation, and was prepared by the arc-discharge method. Arc-grown MWCNTs have relatively uniform structures and typically appear to have less structural defects than MWCNTs synthesized by chemical vapor deposition (CVD), as observed by TEM [22]. The received raw material consists of powdered cathode deposition core material with 30–40% CNT content with the remainder other graphitic particles, at least as stated by MER Corp [23]. Figure 1(a) shows an SEM image of the raw material. The supplier states that these MWCNTs have "8–30 layers, are 6–20 nm in outer diameter, and are 1–5 μm in length" [23].

To increase the MWCNT concentration, the source powder was first dispersed in ethanol (Pure, 200 Proof, Pharmco Products, Inc.) and sonicated in a bath sonicator (Ultrasonic Cleaner Model-175HT, Crest Ultrasonics Corp., Trenton, NJ) for 8 h. It was then left to settle for 8 h and large particles sedimented out. The supernatant was then separated from the sediment by careful pouring, and centrifuged (*Speed 6* setting, 3 min, Marathon Micro-A Centrifuge, Fisher Scientific) twice to further concentrate the CNTs relative to other particles.

A droplet of this ethanol-nanotube mixture was then dispensed onto a plasma-cleaned (Plasmatic Systems Inc., II-862) silicon wafer (2–10 Ohm-cm, P-type, Polished, Polishing Corporation of America). After the ethanol dried, SEM observation [Fig. 1(b)] showed that most of the MWCNTs were separated on the Si wafer, but there were still some graphitic particles present. While chemical oxidation or heat treatment can effectively eliminate small carbon particles [24–27], these processes may form defects in the nanotubes [28], which should lower their strength. In comparison to our earlier work [19; and see also 29–31, which discuss the impact of extensive oxidative treatment and likely defects for the MWCNTs tested in 19], the approach used here has the aim of limiting defects caused by exposure to chemical reactants during processing of the sample, prior to pick up and configuring for mechanical testing.

The long-time exposure to sonication could possibly introduce defects to the MWCNT outer shell; during the course of our work we also attempted to prepare dispersed MWCNTs in ethanol by exposing to bath sonication for only about 10 s. SEM showed that some MWCNTs were separated but a large fraction was still agglomerated with 'graphitic' particles. Tensile tests were performed on MWCNTs prepared with both methods (8 h sonication for #1–9; ~10 s sonication for #10–14). It was not possible to entirely avoid the use of sonication, because the as-received sample was ill-suited for extracting one MWCNT from the agglomerates (for the method employed here to extract MWCNTs for study).

It was found to be important that the MWCNTs be spatially separated from each other for the step of picking one out and configuring it for tensile loading. A copper TEM grid (PELCO®Grids, Ted Pella, Inc.) was cut in half, and was used to 'scratch' the separated MWCNTs on the substrate, yielding MWCNTs adhered to the TEM grid and many protruding from the cut edge [Fig. 1(c)]. This allowed their 'pickup' with AFM tips for subsequent tensile loading using our home-built nanomanipulator.

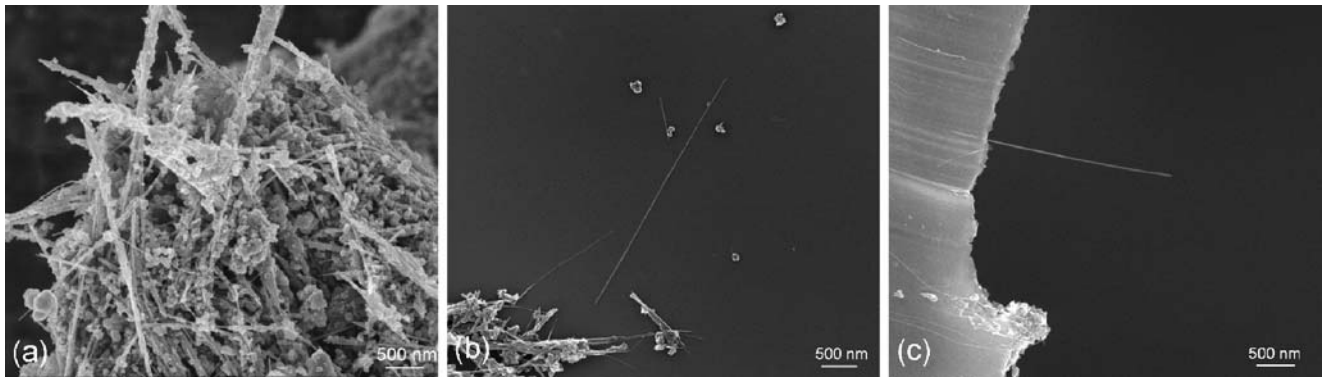

Fig. 1. SEM images of (**a**) MWCNT 'powder' from MER Corp. (**b**) Separated MWCNTs on silicon substrate after fractionation as described in the text. (**c**) A MWCNT at the edge of a cut TEM grid

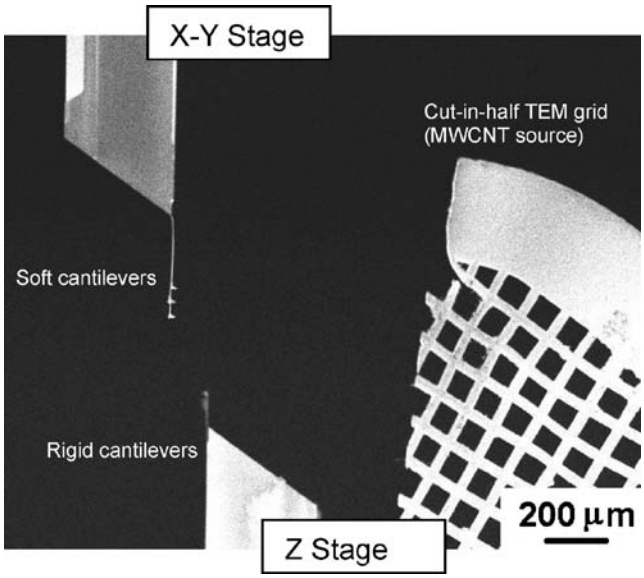

Fig. 2. Low-magnification SEM image showing the experimental setup and the MWCNT source for the nanoscale tensile test

Experimental Setup

Tensile loading of MWCNTs was performed with the nanomanipulator inside the vacuum chamber of an SEM (a LEO-1525 SEM or an FEI Nova-600 SEM). Figure 2 shows the experimental setup. AFM chips were mounted on the two opposing positioning stages of the nanomanipulator. An AFM chip with soft cantilevers (Chip CSC 12, lengths 350 and 300 μm, nominal force constants 0.03 and 0.05 N/m, respectively; MikroMasch, Inc.) was mounted at the end of a piezoelectric bender (Noliac A/S, Denmark, ceramic multilayer bender B1) on the X–Y linear motion stage; and an AFM chip with more rigid cantilevers (Chip NSC 12, lengths 90 and 110 μm, nominal force constants 14.0 and 7.5 N/m, respectively; MikroMasch, Inc.) was mounted on the Z linear motion stage together with the MWCNT source (a cut-in-half TEM grid with MWCNTs attached).

Tensile Testing Process

The 'soft' AFM cantilevers mounted on the X–Y stage serve as force-sensing elements; their force constants were calibrated in situ prior to the test using the resonance method developed by Sader et al. [32]. The resonance frequencies and dimensions of the cantilevers were measured in the SEM, and their force constants thereby obtained. A description of this calibration procedure has been published [33].

To configure an experiment, the source is first inspected and a candidate MWCNT selected. Nanomanipulation then brings the tip of a soft AFM cantilever into contact with the selected MWCNT and a carbonaceous deposit made by the electron beam induced deposition (EBID) method serves as one clamp. The MWCNT is then pulled away from the source and the other end is clamped to the tip of a rigid AFM cantilever, also with the EBID method.

Once a MWCNT was clamped between the two opposing AFM tips [Fig. 3(a)] it was tensile tested. An increasing *dc* voltage incremented in discrete steps was applied to the piezoelectric bender to displace the end of the bender. The soft AFM cantilever (attached to

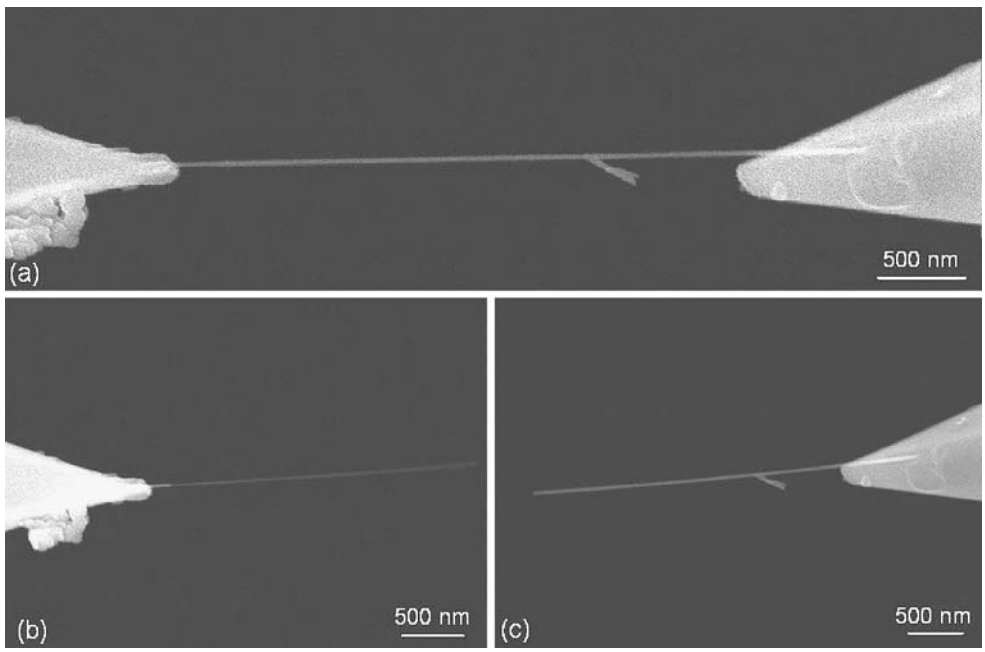

Fig. 3. 'Sword-in-sheath' failure of a MWCNT under tension. (**a**) A MWCNT clamped between two AFM tips and under tension. (**b**) The nanotube fragment with inner shells pulled out ('won' from the opposing fragment). (**c**) The outer shell fragment attached to the opposing AFM tip

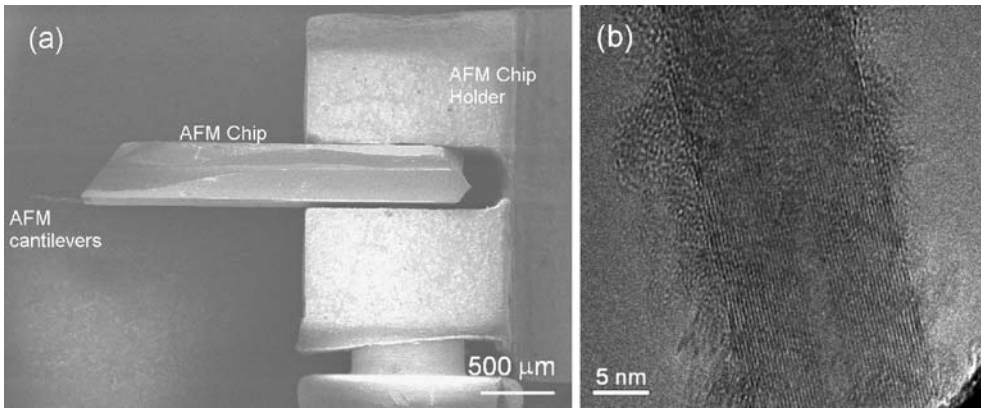

Fig. 4. (**a**) SEM image of an AFM chip in the homemade AFM chip holder. (**b**) TEM image of a portion of a MWCNT fragment attached to the AFM tip

the piezoelectric bender) was thus moved away from the opposing fixed 'rigid' AFM tip. Since the two AFM tips were connected through the MWCNT, the soft cantilever was deflected and a tensile load applied to the specimen. With increased tensile load the MWCNT elongated and then eventually fractured, in a 'sword-in-sheath' manner (Fig. 3).

In our current experimental setup, we do not measure tensile load or the strain directly during the loading process. We record the whole tensile loading experiment by taking a series of SEM images. The tensile load and strain are obtained from image analysis after the experiment is finished. With measurement of the outer shell diameter by TEM, tensile stress is calculated, and thus stress vs. strain is obtained. The tensile strength, maximum strain and modulus of elasticity can, in principle, be thereby evaluated.

Diameter Measurement

Since the MWCNTs tested were only ~10 nm in outer diameter, high-resolution TEM images were acquired to obtain the outer shell diameter of each MWCNT.

TEM imaging of a CNT attached to an AFM tip is non-trivial because the AFM chip is too large for a conventional TEM specimen holder. The AFM chip should be so positioned in the TEM to allow exposure of the CNT at the AFM tip to the electron beam, also impractical in a conventional TEM specimen holder. So, a 'chip holder' was built to put the AFM chip Fig. 4(a) in a TEM single tilt straining holder (Gatan Inc., Model 654) that has a large enough through-region to accommodate this chip holder. A Hitachi HF-2000 TEM was used and measurements were performed at room temperature; because the MWCNT is cantilevered, thermal vibration renders measurement of the diameter far from the clamp impossible. By imaging close to the clamp it is possible to obtain lattice fringes that serve as an internal calibration of the tube diameters. Figure 4(b) shows a TEM image of a portion of a MWCNT fragment. The outer diameter of the nanotube was determined based on the outermost fringes in the TEM image.

One concern about measuring the MWCNT fragment diameters after fracture is that the fragment diameter might differ from the original diameter prior

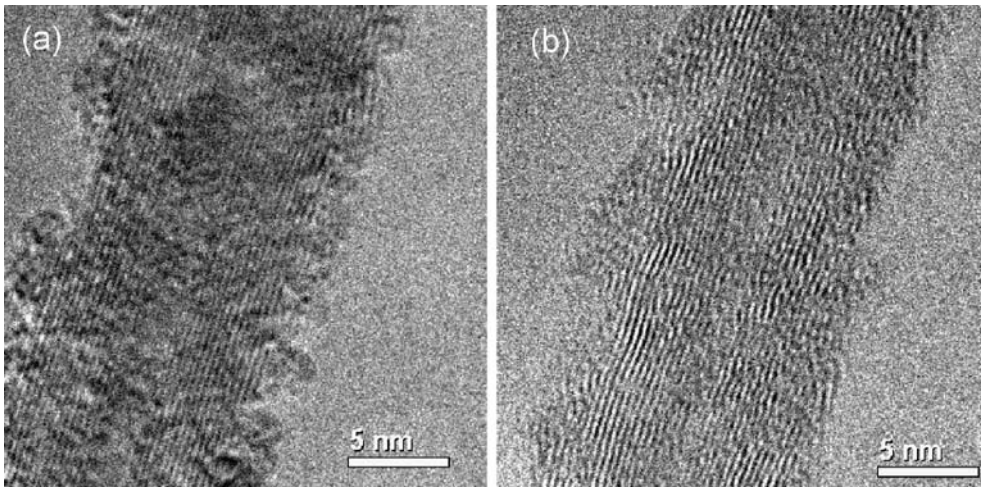

Fig. 5. TEM image of a portion of MWCNT #7 (**a**) before, and (**b**) after tensile testing. Thus, (b) allows for a measurement of the outer diameter of the fragment after fracture, in the same region as the original MWCNT prior to fracture

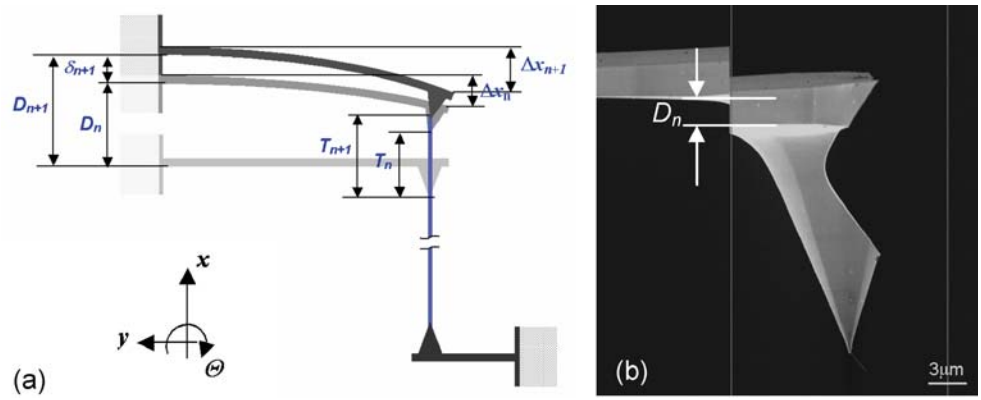

Fig. 6. (**a**) Schematic of piezoelectric bender response calibration. (**b**) The response of an unloaded cantilever to an applied *dc* bias voltage

to specimen fracture. To probe this issue, we first picked up a MWCNT with the AFM tip in the SEM, then without tensile loading measured the diameter in the TEM. The MWCNT was then returned to the SEM, the other end was mounted on the opposing AFM cantilever tip, and the specimen was tensile loaded until it broke. The fragments were then observed in the TEM. Two MWCNTs (#7,8) were tested in this way, and their diameters, as measured before and after the testing, were essentially identical. Figure 5(a) shows the TEM image of MWCNT #7 before, and Fig. 5(b) after, tensile testing.

Data Analysis and Discussion

Force Determination

Direct measurement of the cantilever deflection is challenging due to a lack of a reference point [34], and we use a method to obtain the deflection based on calibration of the piezoelectric bender response as shown in Fig. 6.

As mentioned, the force-sensing cantilever is displaced by actuating the piezoelectric bender. The applied *dc* voltage was increased in constant steps

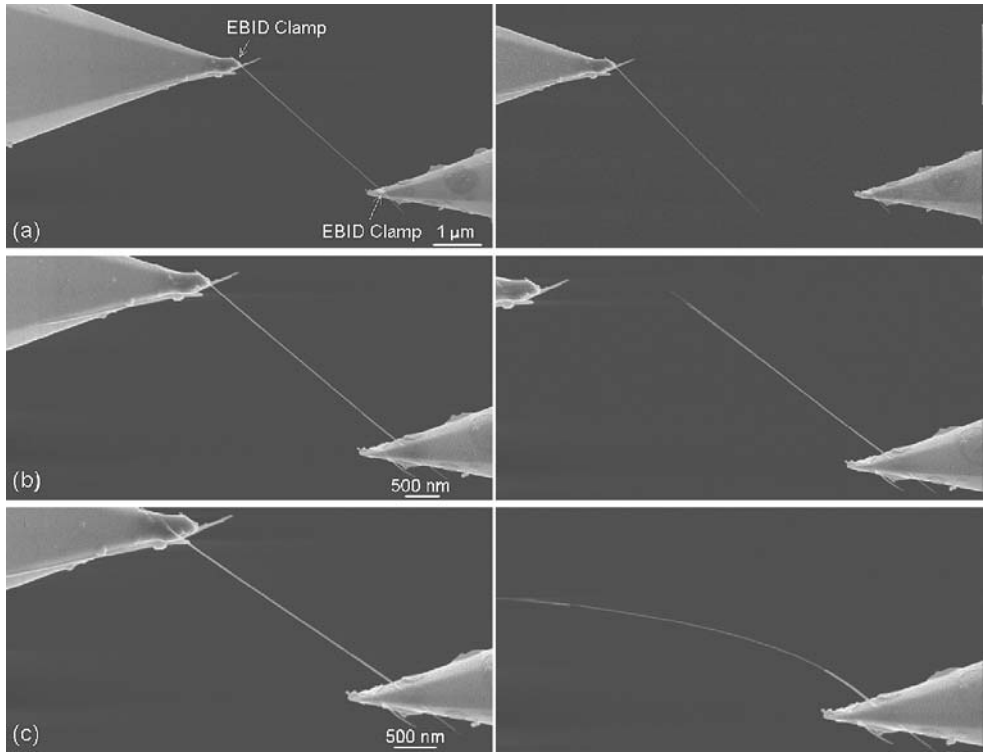

Fig. 7. SEM images showing the results of three sequential tensile tests on the outer shell of MWCNT #6, as described further in the text

(ΔV), which consequently induced an approximately constant increase (δ) of the AFM chip displacement (D). Figure 6(a) shows a schematic of the actuation process. At the nth loading step, the cantilever deflection, Δx_n, can be obtained by subtracting the corresponding AFM tip displacement, T_n, from the AFM chip displacement, D_n, i.e., $\Delta x_n = D_n - T_n$.

The AFM tip displacements (T) were obtained from image analysis. The AFM chip displacements (D) were obtained by calibration as follows. After the tensile test, the same sequence of *dc* voltage steps was applied to the piezoelectric bender, and the displacements of the unloaded cantilever recorded [Fig. 6(b)]. These displacements were experimentally confirmed to be the same as the displacements of the AFM chip (D) during tensile testing. With the AFM chip displacement (D) and AFM tip displacement (T) values, the AFM cantilever deflection (Δx) values were obtained for all loading values.

In our approach the MWCNTs being tested are typically *not* aligned perfectly perpendicular to the cantilevers [Fig. 7(a)]. Furthermore, with the deflection of the cantilever the orientation of the MWCNT changes. The alignment of the specimen at each load is used to obtain the load acting along the MWCNT; the detailed analysis is provided elsewhere [34].

Tensile Stress Calculation

A MWCNT consists of many concentric cylindrical shells. The interaction between the individual shells is assumed to be of the van der Waals type. When a MWCNT is clamped to the AFM tip with the EBID method, only the outermost shell is physically attached to the AFM tip. During tensile testing, the outermost shell is loaded since very little load is transferred to the inner shells [19]. Consequently, only the outermost shell fractures under tension, a picture that is supported by the fit values of the Young's modulus of the outer shells, discussed further below, and from analysis of the contraction of the outermost shell (see Yakobson, private communication,[1] for detail; as discussed therein, a 10-nm diameter outershell can at most exert a pressure of ~700 MPa. This pressure changes the interlayer separation in graphite, e.g., by less than 3% [35, and references therein]). Our data analysis is thus based on the assumption that the outermost shell carries the entire tensile load. The tensile stresses in the outermost shell were calculated by using the interlayer distance 0.34 nm as the thickness of the outermost shell.

As can be seen in the TEM images Figs. 4(b) and 5, there is a thin layer of amorphous carbon deposit on the outer wall of the MWCNT fragments, which is the result of EBID deposition occurring when the specimen was exposed to the electron beam during observation, pick up, mounting, and during the tensile loading experiment in the SEM. EBID has been a useful method for making clamps in our work; however the additional material deposited during observation and testing is undesirable. EBID yields further deposition during TEM imaging as we observed that the amorphous layer gradually became thicker and thicker.

Since the experiment as performed involves *in-situ* SEM observation and there are always residual hydrocarbon molecules present in the SEM, such EBID deposits do occur. The actual thickness of the EBID coating varied for different tubes, depending on the beam exposure time and the SEM vacuum condition. TEM observation revealed that the layer thickness ranged from 1–10 nm. According to our previous work [36], the deposit consists of hydrogenated amorphous carbon having an elastic modulus roughly in the range 30–60 GPa. If the EBID deposit is also bearing load, the tensile stress supported by the outermost shell is overestimated in our analysis, and thus the strength and modulus values would be as well. We are attempting to perform the tensile testing without directly imaging the CNT, to reduce the build-up of amorphous carbon.

Strain Determination

The tensile strain is calculated based on the measured length of the nanotube at each load, from SEM images. The strain measurement accuracy is 0.1–0.2%, based on pixel resolution as discussed in further detail in [34].

As mentioned, MWCNT samples were initially prepared with long periods of sonication. These MWCNTs (#1–9) were tested in the LEO-1525 FEG SEM in a central user facility. Later, MWCNT samples were prepared with only a short time of exposure to

[1] A "Chinese Finger Puzzle" effect is limited by the low friction, if the walls are perfect. Strongly increased binding by radial compression due to Poisson reduction of the outermost shell is unlikely because the resulting pressure is relatively small. E.g., by assuming a perfectly rigid core (simply for the sake of analysis), one can obtain an upper limit estimate of this pressure p, as the outermost shell would, in the absence of a core, shrink by $\varepsilon \cdot \nu$(ε ~0.05 elongation, ν~0.2). Thus, to return the shell to its original diameter (with the presence of a perfectly rigid core) one would have $p < 2C/d \cdot \varepsilon \cdot \nu$ = 690 N/m /10 nm • 0.2 • 0.05 = 0.69 GPa (We assume the value C = 345 N/m in-plane stiffness of graphene (Kudin, K., Scuseria, G. E., Yakobson, B. I., "C_2F,BN, and C Nanoshell Elasticity from *ab initio* Computations". Physical Review B 64:235406 (2001)) and d = 10 nm diameter for this example).

sonication (~10 s, as discussed above, vs. 8 h) and these MWCNTs (#10–14) were tested in a dedicated FEI Nova-600 SEM. The tensile testing experiments were performed in the same way in each SEM, but different methods were used to record the experiment. The tests performed in the LEO SEM were recorded by 'manually' recording SEM images at each loading step. The FEI SEM has a *movie recording function* that can automatically acquire and save a series of SEM images at given time intervals, which we find significantly reduces the time interval between two loading steps. This time interval is around one minute for manual recording but only 5–10 s for automatic recording. As a result, we are able to perform the tensile test at finer loading steps (0.1V voltage increment steps instead of 0.3 V increment steps) and with a shorter overall time (2–5 min) instead of the 10–20 min duration experiments performed in the LEO-1525 SEM.

Since the tensile load is increased in discrete steps and the response of the piezoelectric bender to the applied *dc* voltage is fast (the manufacturer states that the response is in the millisecond range), the smaller time interval between two loading steps is not relevant to the strain rate. In fact, the strain rate is lower for the experiments performed in the Nova-600 SEM because a smaller increment in force was used at each load step. The strain rate is unknown since we do not know the exact response time of the piezoelectric bender, but it should be on the order of 0.1 s^{-1}.

It is important to ensure that there is no slippage at the clamp during the testing process. Should sliding occur at the clamp a larger elongation might be attributed, leading to a lower calculated value for the elastic modulus. In several cases (MWCNT #4–6, 11–12), clamps were deliberately fabricated so that the ends of the MWCNTs projected past the clamp (Fig. 7, for example), and the lengths of the extended portions were monitored. No visible change of this segment length was observed at high-magnification (typically at 50,000, corresponding to ~7 nm per image pixel) through the entire loading process. If slippage of the MWCNT at the clamp occurs, it is negligible.

Tensile Testing Results

Eighteen tensile tests were performed on 14 MWCNTs clamped between two opposing AFM tips; three MWCNTs (and thus, their fragments after fracture) were loaded multiple times. Unlike the previous tests by Yu et al. [19], in which 40 attempts were made but 21 times the clamps themselves detached during loading, the EBID clamps were sufficiently strong that a clamp detached only once (MWCNT #5). (Note that we are not referring to 'slippage' between specimen and clamp, but rather detachment of the whole clamp itself. As mentioned, slippage did not occur.)

Stress concentration due to experimental configuration is a concern in mechanical testing. In macroscopic tensile tests specimen geometries are chosen to reduce stress concentration at the grips. One cannot of course, convert a MWCNT to a 'dog bone' shape, thus pointing to one obvious difference between nanoscale specimens and macro scale specimens. There is, therefore, the possibility of stress concentration at or near the EBID clamps [37]. If the tube is not perfectly aligned between the two AFM tips, then during loading, bending and torsional moments are present that may create further stress concentration at the clamps. Indeed, failure of most of the samples in our previous study on crystalline boron nanowires occurred in the specimen directly at the clamp [34]. Tubes (as opposed to solid rods) are perhaps more 'forgiving' because the majority of the MWCNTs we tested did not fail at the clamps. As discussed shortly, this could also be because of stress concentrations in the gauge length that are larger than near the clamps. Of the 18 tensile tests we performed there were five cases where the nanotubes fractured at the clamps, and the tubes failed at essentially random locations along the gauge length in the other 13 cases. As will be presented later in detail, we believe that the outer shells of these MWCNTs typically contain defects for the lengths loaded, which themselves cause stress concentrations and thus failure. The presence of defects in the outermost shell of a MWCNT can greatly reduce its failure strength [29–31, 38].

Table 1 shows the tensile testing results for these arc-grown MWCNTs. MWCNT #1–9 were from samples prepared with relatively long duration sonication and tested in the LEO-1525 SEM; MWCNT #10–14 were from samples prepared with a few seconds of sonication and were tested in the FEI Nova-600 SEM with automatic video recording. While there are too few tests to claim statistical significance, it is potentially of interest that #10–14 (short time sonication) failed at low stress and strain, compared to #1–9. Further study of this is indicated. For all 18 measurements, the outer shell fracture strengths ranged from 10 to 66 GPa, and their Young's moduli from 620 to 1,200 GPa with an average of 940 GPa. This mean value is close to the theoretical predicted Young's modulus of 1.0 to 1.1 TPa for MWCNTs [4–6].

The measured fracture strengths of these MWCNTs were in the same range as those determined in our previous work for a different sample [19] but the

Table 1 Tensile testing results on fourteen arc-grown MWCNTs

MWCNT number	Length (μm)	Outer diameter (nm)	Breaking force (nN)	Fracture strength (GPa)	Failure strain (%)	Elastic modulus (GPa)
1	1.95 ± 0.01	8.5 ± 0.3	600 ± 31[b]	66 ± 4.4	6.3 ± 0.5	1,100 ± 110
2	2.94 ± 0.01	9.7 ± 0.3	320 ± 17	30 ± 1.9	3.5 ± 0.4	870 ± 100
3	3.53 ± 0.01	19.4 ± 0.3	620 ± 32[d]	34 ± 1.8[d]	4.7 ± 0.3[d]	680 ± 55
4	4.06 ± 0.01	9.8 ± 0.3	120 ± 6.2	12 ± 0.9	1.8 ± 0.3	680 ± 110
5	1.75 ± 0.01	12.7 ± 0.3	140 ± 7.3[c]	10 ± 0.8[c]	1.3 ± 0.3[c]	840 ± 210
6[a]	4.08 ± 0.01	9.7 ± 0.3	420 ± 22	41 ± 2.7	3.0 ± 0.2	1,200 ± 130
7	3.92 ± 0.01	12.7 ± 0.3	200 ± 11	15 ± 0.9	1.0 ± 0.2	1,200 ± 250
8	3.36 ± 0.01	8.9 ± 0.3	300 ± 16[d]	31 ± 2.2[d]	2.7 ± 0.2[d]	1,200 ± 120
9[a]	6.12 ± 0.01	5.0 ± 0.3	110 ± 5.8	21 ± 2.7	3.5 ± 0.2	620 ± 85
10[a]	4.71 ± 0.01	9.4 ± 0.3	140 ± 7.1	14 ± 1.0	1.1 ± 0.2	1,200 ± 210
11	4.08 ± 0.01	10 ± 0.3	130 ± 6.6[b]	12 ± 0.8	1.8 ± 0.2	730 ± 100
12	3.31 ± 0.01	10.7 ± 0.3	200 ± 10	17 ± 1.1	1.8 ± 0.2	960 ± 140
13	1.49 ± 0.01	12.0 ± 0.3	250 ± 13	19 ± 1.4	2.4 ± 0.3	890 ± 140
14	7.97 ± 0.01	13.8 ± 0.3	240 ± 12	16 ± 0.9	1.2 ± 0.2	1,200 ± 190

[a] These nanotubes were loaded multiple times. The length listed is the initial length. All other parameters are from the final test
[b] Failed at the clamps
[c] The clamp itself failed during the test so these are lower bounds of the fracture stress and failure strain for MWCNT #5
[d] Up to the linear limit. As discussed in the text (below), the failure strains of MWCNT #3 and #8 were larger

measured failure strains are significantly lower. There are perhaps similar types of defects, but much less of them along the gauge length, for the current sample which was not processed by an extensive oxidative treatment as the former sample [19; and see discussion in 29–31].

Multiple Tensile Loading Experiments

Since the MWCNTs studied here have an outer diameter of ~10 nm, defects consisting of clusters of missing atoms will have a considerable effect on the tensile strength. For example, removing sets of adjacent atoms along the circumference of a SWCNT can greatly reduce its fracture strength and failure strain, at least per modeling results [29–31, 38]. For example, computational modeling shows that one- and two-atom vacancy defects reduce the failure stresses of pristine tubes by as much as 26% and the failure strains by as much as a factor of two [30].

Either all the arc-grown MWCNTs we tested contain structural defects prior to being configured for testing, or something in the testing process itself is inducing defects—otherwise a relatively constant value for fracture strength would have been observed for all 18 values. Theory suggests that defect-free CNTs should fail at higher strains (>10%) when loaded in tension [5, 39], but the outer shells of the MWCNTs we tested fractured at strains of 1–6% (Table 1).

When these defected nanotubes were tensile loaded, it might be expected that they should fail at the 'critical flaw' present in the outermost shell in the gauge length, or perhaps at one of the two clamps, in short wherever the stress concentration is largest. One or both of the fragments of a MWCNT that does not fail at its clamp might then be able to sustain a higher tensile load since it might contain less significant defects than the original specimen. Repeated testing should be capable of probing this issue and so we conducted multiple tensile tests on three MWCNTs (#6, 9,10). Figure 7 shows SEM images of three tensile tests performed on the outermost shell of MWCNT #6. In the first test fracture happened near the 'right clamp'. The fragment of the outer shell was then re-clamped to the AFM tip on 'the right' and a second tensile test performed in which the outer shell fractured near the 'left clamp'. The outer shell fragment was then clamped to the AFM tip on 'the left' and loaded a third time leading to fracture roughly in the middle.

Table 2 shows the results for this sequence of tensile loading experiments on the outer shell of MWCNT #6 (and MWCNTs #9,10). There is only a slight increase in the force at failure between the first and second tensile tests but a significant increase between the second and third. Note that this particular MWCNT was not well aligned, and such misalignment resulted in bending and torsional loads that likely caused higher stress concentration at the clamp [37]. It seems likely that the stress concentration at the clamps led to the fracture of this nanotube in the first two tests. In the third test the nanotube failed in the middle, at a higher breaking force. Figure 8 shows the stress-strain rela-

Table 2 Multiple tensile testing results on the outer shell of three nanotubes

Sample number	Test number	Gauge length (μm)	Outer diameter (nm)	Breaking force (nN)	Fracture strength (GPa)	Failure strain (%)	Elastic modulus (GPa)
MWCNT	1	4.08 ± 0.01	9.7 ± 0.3	220 ± 11*	21 ± 1.4	1.8 ± 0.3	1,200 ± 210
#6	2	3.75 ± 0.01	9.7 ± 0.3	240 ± 12*	23 ± 1.4	1.9 ± 0.3	1,250 ± 210
	3	3.46 ± 0.01	9.7 ± 0.3	420 ± 22	41 ± 2.6	3.0 ± 0.2	1,230 ± 130
MWCNT	1	6.12 ± 0.01	5.0 ± 0.3	74 ± 3.8	14 ± 1.8	2.4 ± 0.2	650 ± 100
#9	2	3.13 ± 0.01	5.0 ± 0.3	110 ± 5.7	21 ± 2.7	3.5 ± 0.2	620 ± 87
MWCNT	1	4.71 ± 0.01	9.4 ± 0.3	82 ± 4.3*	8.2 ± 0.6	0.7 ± 0.2	1,100 ± 200
#10	2	4.58 ± 0.01	9.4 ± 0.3	140 ± 7.3	14 ± 1.0	1.1 ± 0.2	1,150 ± 210

* Failed at the clamps

tionships of the three tests. The elastic moduli obtained from a linear fit of each of the stress-strain curves are similar in all three tests. For the cases where nanotubes fractured near the clamps, the fracture strengths measured are likely to be lower than their true values.

As shown by Li et al. [37] the stress condition at a clamp depends on several parameters such as the angle of misalignment, the thickness of the clamp material between the nanotube and the AFM tip surface, and others. While the angles of misalignment were more or less the same for all three cases, there are some differences in the clamp geometries. As shown in Fig. 7(b), the new 'right clamp' is larger than the old one in Fig. 7(a). The new 'left clamp' Fig. 7(c) is also larger than the old one. In addition, it is also made on top of an EBID layer that may reduce the extent of stress concentration [37]. Perhaps the new clamps reduced stress concentration at both clamps, which eventually resulted in the fracture of the nanotube at its 'critical flaw' instead.

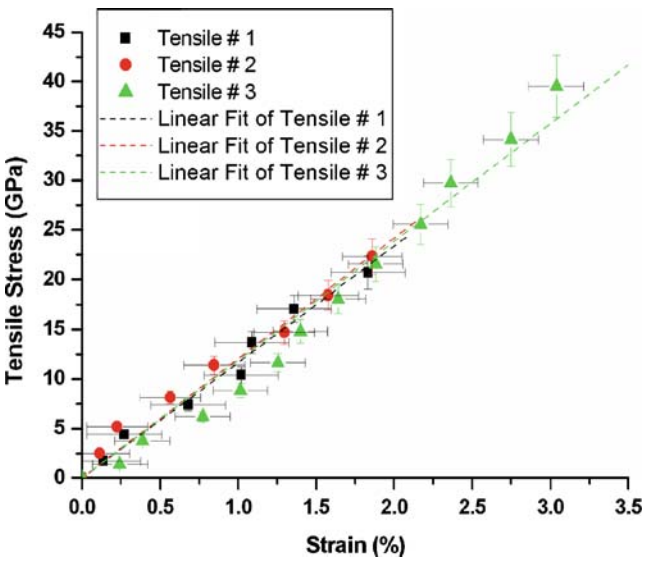

Fig. 8. The stress-strain relationships from the three tensile tests on MWCNT #6

Figure 9 shows SEM images of two tensile tests performed on MWCNT #9. As can be seen, this nanotube is well aligned between the two opposing AFM tips. The fact that in both tests the nanotube fractured somewhere in the middle further suggests that specimen alignment may influence the stress concentration at the clamps. An increase in both the fracture strength and failure strain between the first and second test was observed (Table 2).

Unfortunately these arc-grown MWCNTs are relatively short, at least for the method used here, which limits the number of tests that can be practically performed on the same outermost shell.

Yielding

Yielding of material, i.e., a considerable elongation of the specimen with no noticeable increase in the tensile load, is commonly observed in tensile tests on ductile materials. Simulation shows that the yielding of CNTs depends on the activation and propagation of defects and the tube structure [39, 40]. For example, large-scale molecular dynamics simulation by Nardelli et al. [39] led to the authors concluding that a SWCNT under tension can have either plastic or brittle response, depending on the testing conditions and tube chirality. Brittle failure of a (20,0) CNT was observed in the simulation work of Belytschko et al. [29].

In our tensile testing experiments, apparent 'yielding' was observed for two nanotubes (MWCNT #3, 8) while others were found to have essentially linear stress vs. strain up to fracture. As shown in Fig. 10, there were large increases in strain at the last loading steps.

It is possible that these nanotubes were fractured but the two segments were not completely separated, which would lead to a sudden increase in the total length [as for the case shown in Fig. 9(a)]. Yu et al. [41] performed sliding tests on two MWCNTs fragments that remained in contact after failure. The maximum interaction forces reported were 152 and

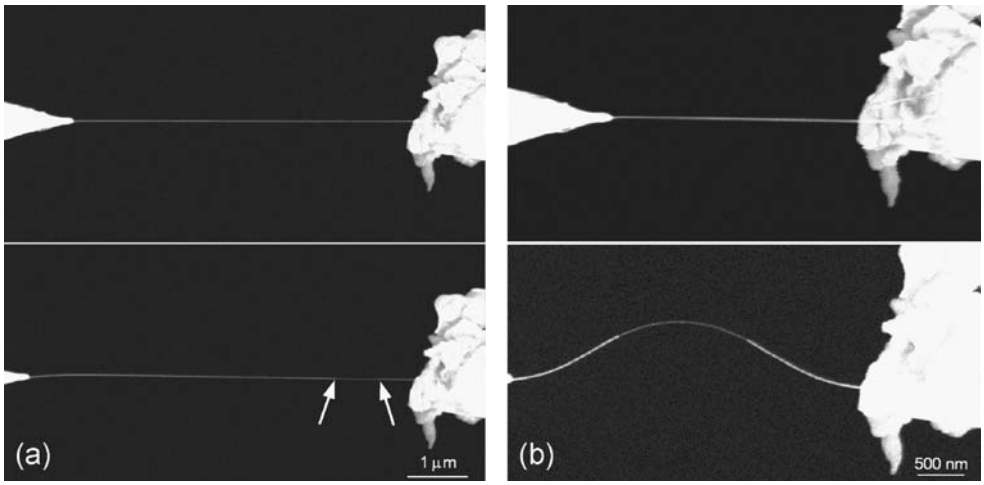

Fig. 9. (**a**) First and (b) second tensile test on MWCNT #9. (the locations where the outer shell fractured are marked in (a))

219 nN with initial contact lengths of 2.2 and 7.5 μm, respectively. In our case, the corresponding load at the steps of 'yield' for MWCNT's #3 and #8 are 620 and 300 nN, and the length of the exposed inner shells after fracture are only 460 and 730 nm, respectively. Therefore, the observed elongation is unlikely to be the result of sudden fracture of the outermost shell and then 'shell sliding interaction'.

Yielding of ductile material can be easily detected by tensile loading at a constant strain rate. Our nanoscale tensile testing is performed instead at an approximately constant stress rate and thus as performed, was unsuitable for unambiguously detecting yielding. As previously discussed, the *dc* voltage applied to the bender was increased in constant steps, which induced an increase in the deflection of the force-sensing cantilever in approximately constant steps. At each loading step the increase of the nanotube length (10–20 nm) is normally far less than the increase of cantilever deflection (100–300 nm) at that step. As a result, the tensile load applied to the nanotube increased in approximately constant steps.

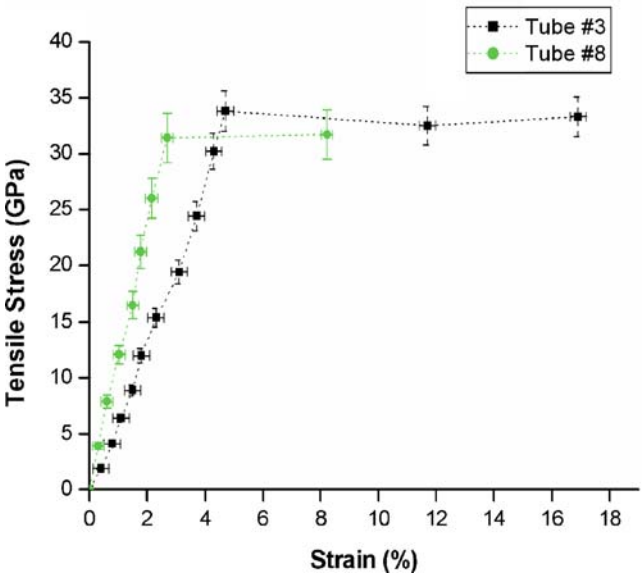

Fig. 10. Stress-strain relationships of MWCNT #3 and #8 from tensile loading

The occurrence of yielding (in our experiment) should lead to a sudden increase of the nanotube length. If the increase of nanotube length exceeds the increment of cantilever deflection at that step, the tensile load applied to the specimen is actually decreased in our experiment. So, the nanotube may not immediately fracture, which may allow capture of an SEM image. However, if the increase of nanotube length is less than the increment of cantilever deflection at that step, there is still an increase in the tensile load, which may lead to the sudden fracture of the nanotube before any SEM image can be acquired. The cantilever deflection step used in the tensile testing of MWCNT #1–9 was 250–300 nm. Considering the nanotubes tested were between 2–6 μm in length, a 250–300 nm increase in length requires a 4–15% elongation. Thus we would only expect to capture images of large magnitude yielding.

This is the first time we observed the apparent 'yielding' of a nanostructure under tension. The other nanostructures we have studied, such as crystalline boron nanowires [34], carbon nanofibers [42] and templated carbon nanotubes [43], all failed at low strain in a brittle manner. Relatively large loading steps were used in those tests, and thus any yielding of nanostructures if present, was not captured. In principle, the yielding of a nanostructure can be detected if we adopt small enough loading steps. This is a future direction for our work; with our existing power supply we can input significantly smaller increments in the voltage applied to the piezoelectric bender.

Conclusion

The fracture strength and elastic modulus of individual MWCNTs synthesized with the arc-discharge method and received from a commercial supplier were obtained by force-displacement measurements with our multi-degree of freedom nanomanipulator inside an SEM. Eighteen tensile tests were performed on 14 MWCNTs with three being tested multiple times. For accurate diameter measurement, an AFM chip holder was used that enabled direct transfer of the MWCNT specimens from SEM to TEM. Tensile stress was calculated assuming the outermost shell of the nanotube carried the entire load, based on the observed 'sword in sheath' fracture. The measured fracture strength of the outermost shell of 14 nanotubes ranged from 10 to 66 GPa. The Young's moduli of the nanotubes obtained from linear fit of the stress-strain curves were from 620 to 1,200 GPa with an average value of 940 GPa. Stress concentration at the clamps remains a concern for such measurements. Apparent 'yielding' of two nanotubes was observed, in contrast to the other 16 measurements that indicated brittle fracture.

Acknowledgments We thank S. Mielke for comments. This work is supported by the National Science Foundation (NIRT Program, Grant No. 0304506, Dr. Ken P. Chong, Program Director) and by the NASA BIMat URETI # NCC-1-02037. The SEM (partially) and TEM work was performed in the EPIC facility of NUANCE Center which is supported by NSF-NSEC, NSF-MRSEC, Keck Foundation, the State of Illinois, and Northwestern University.

References

1. Iijima S (1991) Helical microtubules of graphitic carbon. Nature 354(6348):56–58.
2. Iijima S, Ichihashi T (1993) Single-shell carbon nanotubes of 1-nm diameter. Nature 363(6430):603–605.
3. Bethune DS, Kiang CH, Devries MS, Gorman G, Savoy R, Vazquez J, Beyers R (1993) Cobalt-catalyzed growth of carbon nanotubes with single-atomic-layer walls. Nature 363(6430):605–607.
4. Ruoff RS, Lorents DC (1995) Mechanical and thermal properties of carbon nanotubes. Carbon 33(7):925–930.
5. Yakobson BI, Brabec CJ, Bernholc J (1996) Nanomechanics of carbon tubes: instabilities beyond linear response. Phys Rev Lett 76(14):2511–2514.
6. Lu JP (1997) Elastic properties of carbon nanotubes and nanoropes. Phys Rev Lett 79(7):1297–1300.
7. Bower C, Zhu W, Shalom D, Lopez D, Chen LH, Gammel PL, Jin S (2002) On-chip vacuum microtriode using carbon nanotube field emitters. Appl Phys Lett 80(20):3820–3822.
8. Cao H, Wang Q, Wang DW, Dai HJ (2005) Suspended carbon nanotube quantum wires with two gates. Small 1(1):138–141.
9. Javey A, Tu R, Farmer DB, Guo J, Gordon RG, Dai HJ (2005) High performance n-type carbon nanotube field-effect transistors with chemically doped contacts. Nano Lett 5(2):345–348.
10. Qian D, Dickey EC, Andrews R, Rantell T (2000) Load transfer and deformation mechanisms in carbon nanotube-polystyrene composites. Appl Phys Lett 76(20):2868–2870.
11. Thostenson ET, Ren ZF, Chou TW (2001) Advances in the science and technology of carbon nanotubes and their composites: a review. Compos Sci Technol 61(13):1899–1912.
12. Ding W, Eitan A, Fisher FT, Chen X, Dikin DA, Andrews R, Brinson LC, Schadler LS, Ruoff RS (2003) Direct observation of polymer sheathing in carbon nanotube-polycarbonate composites. Nano Lett 3(11):1593–1597.
13. Treacy MMJ, Ebbesen TW, Gibson JM (1996) Exceptionally high young's modulus observed for individual carbon nanotubes. Nature 381(6584):678–680.
14. Krishnan A, Dujardin E, Ebbesen TW, Yianilos PN, Treacy MMJ (1998) Young's modulus of single-walled nanotubes. Phys Rev B 58(20):14013–14019.
15. Poncharal P, Wang ZL, Ugarte D, de Heer WA (1999) Electrostatic deflections and electromechanical resonances of carbon nanotubes. Science 283(5407):1513–1516.
16. Wang ZL, Poncharal P, de Heer WA (2000) Measuring physical and mechanical properties of individual carbon nanotubes by in situ TEM. J Phys Chem Solids 61(7):1025–1030.
17. Salvetat JP, Kulik AJ, Bonard JM, Briggs GAD, Stockli T, Metenier K, Bonnamy S, Beguin F, Burnham NA, Forro L (1999) Elastic modulus of ordered and disordered multiwalled carbon nanotubes. Adv Mater 11(2):161–165.
18. Salvetat JP, Briggs GAD, Bonard JM, Bacsa RR, Kulik AJ, Stockli T, Burnham NA, Forro L (1999) Elastic and shear moduli of single-walled carbon nanotube ropes. Phys Rev Lett 82(5):944–947.
19. Yu MF, Lourie O, Dyer MJ, Moloni K, Kelly TF, Ruoff RS (2000) Strength and breaking mechanism of multiwalled carbon nanotubes under tensile load. Science 287(5453):637–640.
20. Yu MF, Files BS, Arepalli S, Ruoff RS (2000) Tensile loading of ropes of single wall carbon nanotubes and their mechanical properties. Phys Rev Lett 84(24):5552–5555.
21. Yu MF, Dyer MJ, Skidmore GD, Rohrs HW, Lu XK, Ausman KD, Von Ehr JR, Ruoff RS (1999) Three-dimensional manipulation of carbon nanotubes under a scanning electron microscope. Nanotechnology 10(3):244–252.
22. Lukic B, Seo JW, Bacsa RR, Delpeux S, Beguin F, Bister G, Fonseca A, Nagy JB, Kis A, Jeney S, Kulik AJ, Forro L (2005) Catalytically grown carbon nanotubes of small diameter have a high young's modulus. Nano Lett 5(10):2074–2077.
23. http://www.mercorp.com/mercorp/nano.pdf.
24. Morishita K, Takarada T (1998) Purification of carbon nanotube by wet oxidation. Kagaku Kogaku Ronbunshu 24(4):670–674.
25. Park YS, Choi YC, Kim KS, Chung DC, Bae DJ, An KH, Lim SC, Zhu XY, Lee YH (2001) High yield purification of multiwalled carbon nanotubes by selective oxidation during thermal annealing. Carbon 39(5):655–661.
26. Sun XG, Zeng XS (2004) An investigation on the purification of multiwall carbon nanotubes by oxidation in air. New Carbon Materials 19(1):65–68.
27. Wiltshire JG, Khlobystov AN, Li LJ, Lyapin SG, Briggs GAD, Nicholas RJ (2004) Comparative studies on acid and thermal based selective purification of HiPCO produced

single-walled carbon nanotubes. Chem Phys Lett 386(4–6): 239–243.
28. Bom D, Andrews R, Jacques D, Anthony J, Chen BL, Meier MS, Selegue JP (2002) Thermogravimetric analysis of the oxidation of multiwalled carbon nanotubes: evidence for the role of defect sites in carbon nanotube chemistry. Nano Lett 2(6):615–619.
29. Belytschko T, Xiao SP, Schatz GC, Ruoff RS (2002) Atomistic simulations of nanotube fracture. Phys Rev B 65(23):235430.
30. Mielke SL, Troya D, Zhang S, Li JL, Xiao SP, Car R, Ruoff RS, Schatz GC, Belytschko T (2004) The role of vacancy defects and holes in the fracture of carbon nanotubes. Chem Phys Lett 390(4–6):413 – 420.
31. Zhang SL, Mielke SL, Khare R, Troya D, Ruoff RS, Schatz GC, Belytschko T (2005) Mechanics of defects in carbon nanotubes: atomistic and multiscale simulations. Phys Rev B 71(11):115403.
32. Sader JE, Larson I, Mulvaney P, White LR (1995) Method for the calibration of atomic-force microscope cantilevers. Review of Scientific Instruments 66(7):3789–3798.
33. Chen XQ, Zhang SL, Wagner GJ, Ding WQ, Ruoff RS (2004) Mechanical resonance of quartz microfibers and boundary condition effects. J Appl Physi 95(9):4823 – 4828.
34. Ding W, Calabri L, Chen X, Kohlhaas KM, Ruoff RS (2006) Mechanics of crystalline boron nanowires. Compos Sci Technol 66:1109–1121.
35. Boettger JC (1997) All-electron full-potential calculation of the electronic band structure, elasstic constants, and equation of state for graphite. Phys Rev B 55(17):11202–11211.
36. Ding W, Dikin DA, Chen X, Wang X, Li X, Piner R, Ruoff RS, Zussman E (2005) Mechanics of hydrogenated amorphous carbon deposits from electron beam induced deposition of a paraffin precursor. J Appl Physi 98:014905.
37. Li CY, Ruoff RS, Chou TW (2005) Modeling of carbon nanotube clamping in tensile tests. Compos Sci Technol 65(15–16):2407–2415.
38. Pugno NM, Ruoff RS (2004) Quantized fracture mechanics. Philos Mag 84(27):2829–2845.
39. Nardelli MB, Yakobson BI, Bernholc J (1998) Brittle and ductile behavior in carbon nanotubes. Phys Rev Lett 81(21):4656 – 4659.
40. Yakobson BI (1998) Mechanical relaxation and "intramolecular plasticity" in Carbon Nanotubes. Appl Phys Lett 72(8):918 – 920.
41. Yu MF, Yakobson BI, Ruoff RS (2000) Controlled sliding and pullout of nested shells in individual multiwalled carbon nanotubes. J Phys Chem B 104:8764–8767.
42. Zussman E, Chen X, Ding W, Calabri L, Dikin DA, Quintana JP, Ruoff RS (2005) Mechanical and structural characterization of electrospun PAN-derived carbon nanofibers. Carbon 43:2175–2185.
43. Lu S, Guo Z, Ding W, Ruoff RS (2006) Analysis of a microelectromechanical system testing stage for tensile loading of nanostructures. Review of Scientific Instruments 77(5):1 – 4.